



# Theoretical Study for Dynamic Strain Aging in Niobium: Effect of Temperature and Strain Rate on the Flow Stress

Yooseob Song<sup>1</sup> · William Peterson<sup>1</sup>

Received: 11 August 2020 / Accepted: 13 October 2020 / Published online: 27 November 2020  
© The Korean Institute of Metals and Materials 2020

## Abstract

A constitutive model for niobium with the effect of dynamic strain aging is proposed. The crystal structure of metals hugely influences the dynamic strain aging phenomenon and causes considerable alterations in the material's macroscopic mechanical responses. Dynamic strain aging needs to be accounted for in a constitutive model to obtain accurate predictions of material's thermo-mechanical behaviors during deformation. The proposed constitutive model attempts to describe the material's flow stress responses during deformation by separating the flow stress contributions into the athermal component, thermal component, and dynamic strain aging component. Two different mathematical equations are proposed to model the dynamic strain aging component. The proposed model attempts to describe the mechanical response of niobium for a wide range of strain rates: from quasi-static loading ( $\dot{\epsilon} = 0.001 \text{ s}^{-1}$ ) to dynamic loading ( $\dot{\epsilon} = 3300 \text{ s}^{-1}$ ) across the temperature ranges 77 K–800 K.

**Keywords** Constitutive model · Niobium · Dynamic strain aging · Strain rate effect · Thermal effect

## 1 Introduction

Dynamic strain aging (DSA) is a phenomenon that induces strain hardening in metallic materials at specific temperature ranges. Strain rate and temperature are the main factors that influence flow stress during the deformation process. A rise in temperature generally causes a decline in the flow stress. However, there are temperature ranges where flow stress increases with the increase in temperature as shown in Fig. 1. As the temperature continues to rise, flow stress increases and then starts to decline. As a result, a bell-shaped peak is formed. The maximum stress caused by DSA is dependent on the strain rate, total strain, and the temperature range where DSA occurs. In other words, DSA is observed at distinct combinations of temperature and strain rate ranges. From the data in Nemat-Nasser and Guo [1], DSA was observed at  $400 \text{ K} \lesssim T \lesssim 800 \text{ K}$  under  $\dot{\epsilon} = 0.001 \text{ s}^{-1}$ , but it was not observed at all at this temperature range under  $\dot{\epsilon} = 3300 \text{ s}^{-1}$  and  $\dot{\epsilon} = 8000 \text{ s}^{-1}$ . The temperature range where DSA manifests itself is heavily affected by the crystal

structure of metals. It is also observed that metals with identical crystal structure even may have different responses.

Nemat-Nasser and coworkers have conducted extensive studies of the thermomechanical behaviors of body-centered cubic (bcc) and face-centered cubic (fcc) metals [1–4]. This work focuses on the experimental data from the study of DSA on niobium conducted by Nemat-Nasser and Guo [1]. Samples of niobium were subjected to quasi-static and dynamic loading under a large range of temperatures to investigate the plastic deformation mechanisms. Nemat-Nasser and Guo [1] proposed a constitutive model in their work to describe niobium's macroscopic behaviors under dynamic loading, however, this model did not consider the effect of DSA. To our knowledge, the plastic deformation of niobium with the consideration of DSA over a wide range of strain rates (quasi-static and dynamic) and temperatures has not been captured with a reasonable constitutive model. The constitutive model for niobium presented in this work includes considerations for thermo-mechanical behavior, the behavior of dislocations, separation of the flow stress into three components [DSA ( $\sigma_D$ ), thermal ( $\sigma_{th}$ ), and athermal ( $\sigma_a$ )], and application of the probability function to correlate model predictions with the experimental results. Using the experimental work conducted by Nemat-Nasser and Guo [1],

✉ Yooseob Song  
yooseob.song@utrgv.edu

<sup>1</sup> Department of Civil Engineering, The University of Texas  
Rio Grande Valley, Edinburg, TX 78539, USA

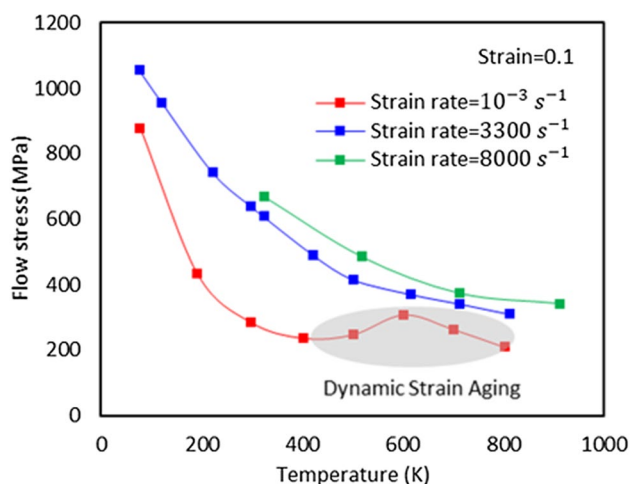


**Fig. 1** Experimental stress–temperature graph for niobium at a strain ( $\epsilon$ ) level of 0.1 with three different strain rates ( $\dot{\epsilon}$ ) [1]. DSA is only observed in the case of  $\dot{\epsilon} = 0.001 \text{ s}^{-1}$

the components of the proposed model were adjusted and substantiated to produce accurate model predictions.

Meanwhile, dislocation density tends to decline as temperature increases. However, this is not always the case, as shown in the experiments by Keh et al. [5] and model predictions by Bergstrom and Roberts [6]. Dislocation density can be described as a function of the equivalent plastic strain [6]. Also, the terms  $U - A$  ( $U$ : dislocation immobilization or annihilation rate;  $A$ : annihilation rate of the mobile dislocations) and  $\Omega$  (probability of annihilation of immobile dislocations) are heavily dependent on the temperature of the material during the deformation process [5, 6]. These terms are further defined in Sect. 2.2. A probability density-shaped function is employed to provide a more reasonable model for the effects of DSA, and the component  $\sigma_D$  is described as a function of three factors: temperature  $T$ , equivalent plastic strain  $\epsilon_p$ , and its rate  $\dot{\epsilon}_p$ ; this is also further described in Sect. 2.2. The range of elastic deformation in the data used for this work is assumed to be negligible, therefore,  $\epsilon = \epsilon_p$  and  $\dot{\epsilon} = \dot{\epsilon}_p$  are assumed.

The model developed by Voyiadjis and Abed (VA model) is used in this study to describe the athermal and thermal components of the constitutive model without DSA, i.e.  $\sigma_{VA} = \sigma_a + \sigma_{th}$  [7]. To account for the DSA component, two mathematical models, ‘Proposed Model I (PM I)’ and ‘Proposed Model II (or PM II)’ will be implemented. The proposed models include the three components discussed previously, i.e.  $\sigma_{PMI,II} = \sigma_a + \sigma_{th} + \sigma_D$ . This paper will present the two models and describe their development. Section 2 presents the mathematical terms in the proposed models for the DSA, thermal and athermal components. The parameters used to describe Niobium’s physical properties used in the PM I and PM II are discerned in Sect. 3 using the experimental data

performed by Nemat-Nasser and Guo [1]. Section 4 will explore the relationship between true stress and true strain to examine the hardening effects of DSA. Section 5 discusses the strain rate sensitivity of the DSA phenomenon in niobium.

## 2 Constitutive Models

A constitutive model that does not consider the DSA element will underestimate the flow stress values in the range where DSA occurs. Increases in temperature, such as those that may be experienced in dynamic manufacturing processes, can result in a greater underestimation of the flow stress. The microstructural features of materials may play a crucial role in the physical characteristics of DSA as well as the dislocation behavior, therefore they have to be accounted for to produce an accurate model [8–12]. Section 2.1 formulates the flow stress in terms of athermal and thermal components based on the physical microstructural properties of the bcc crystal structure. The DSA component is formulated in Sect. 2.2 based on the author’s previous works [9–12].

The VA model for metals with the bcc structure will be applied to characterize the plastic deformation behavior of niobium under both quasi-static and dynamic strain rates at a wide temperature range. The deformation mechanism in the bcc metallic crystalline structures is credited to the relationship between the short-range interactions (known as Peierls barriers) caused by the crystal structure and dislocation motions. As a result, temperature and strain rate are the main factors that determine the thermal yield stress in bcc metals, however, they are not major factors in the hardening process. The formulation of the proposed models considers the relationships between these factors.

### 2.1 Athermal and Thermal Stress Components

By studying the dislocation dynamics of metals (interaction, multiplication, and motion of dislocations), accurate models with the physical characteristics of the metal can be established.

Orowan’s equation describes the plastic shear strain rate,  $\dot{\gamma}^p$ , as follows:

$$\dot{\gamma}^p = b \rho_m v \quad (1)$$

where  $b$  represents the Burgers vector,  $\rho_m$  represents the density of mobile dislocations, and  $v$  represents the average velocity of mobile dislocations.

The plastic shear strain rate,  $\dot{\gamma}^p$ , is related by Eq. (2) to the macroscale plastic strain rate tensor [13].

$$\dot{\epsilon}_{ij}^p = \dot{\gamma}^p M_{ij} \quad (2)$$

where  $\dot{\epsilon}_{ij}^p$  is the macroscale plastic strain rate tensor.  $M_{ij}$ , the symmetric Schmidt orientation tensor, is described by the following expression.

$$M_{ij} = \frac{1}{2}(n_i \otimes s_j + s_i \otimes n_j) \tag{3}$$

where the term  $\mathbf{s}$  describes the unit vector in the slip direction and  $\mathbf{n}$  the unit vector normal to the slip plane.

By combining Eqs. (1) and (2), the equivalent plastic strain rate,  $\dot{\epsilon}_p$ , can be defined as

$$\dot{\epsilon}_p = \sqrt{\frac{2}{3} \dot{\epsilon}_{ij}^p \dot{\epsilon}_{ij}^p} = \bar{m} b \rho_m v \tag{4}$$

where  $\bar{m} = \sqrt{2M_{ij}M_{ij}/3}$  expresses the Schmidt orientation factor.

Dislocation density and equivalent plastic strain are related as follows [14]:

$$\frac{\partial \rho}{\partial \epsilon_p} = M - k_a(\rho - \rho_i) \tag{5}$$

where  $k_a$  denotes the annihilation factor which is dependent on temperature and strain rate.  $\rho_i$  denotes the initial dislocation density and  $\rho$  denotes the total dislocation density. The multiplication factor,  $M$ , is defined by  $M = 1/bl$ , and  $l$  describes the dislocation mean free path.

The term  $v$  (average dislocation velocity) can be formulated with the thermally activated mechanism [12]. The following expression uses the well-known Arrhenius equation [15] to express the average dislocation velocity in this work [13].

$$v = v_0 \exp\left(-\frac{G}{kT}\right) \tag{6}$$

where  $v_0$  is defined as the referential velocity of a dislocation and  $v_0 = d/t_w$ . The term  $d$  indicates the average distance that a dislocation travels between obstacles. The Boltzman’s constant is represented by  $k$  and  $T$  denotes the temperature in Kelvin. The term  $G$  represents the activation free energy, which may be influenced by the internal structure and the shear stress. The activation energy  $G$  can be related to the thermal flow stress  $\sigma_{th}$  as follows [16]:

$$G = G_0 \left(1 - \left(\frac{\sigma_{th}}{\hat{\sigma}}\right)^p\right)^q \tag{7}$$

where  $p$  and  $q$  describe the Peierls barriers.  $G_0$  depicts the referential Gibbs energy.

The thermal component  $\sigma_{th}$  can be formulated using Eq. (7) and the substitution of Eqs. (5) and (6) into Eq. (4) as follows:

$$\sigma_{th} = \hat{\sigma} \left(1 - \left(\beta_1 T - \beta_2 T \ln \frac{\dot{\epsilon}_p}{\dot{\epsilon}_p^0}\right)^{\frac{1}{q}}\right)^{\frac{1}{p}} \tag{8}$$

where  $\dot{\epsilon}_p^0$  represents the referential equivalent plastic strain rate.

Furthermore,  $\beta_1$  and  $\beta_2$  can be expressed as follows:

$$\beta_1 = \frac{k}{G_0} \ln \left( \frac{\bar{m} b^2 \rho_m v_0}{b - \bar{m} d (\lambda_1 - b^2 \lambda_2 \rho_m - b \lambda_3 \rho_f^{0.5})} \right) \tag{9}$$

$$\beta_2 = \frac{k}{G_0} \tag{10}$$

where the term  $\rho_f$  denotes the forest dislocation density. The coefficients  $\lambda_i (i = 1 - 3)$  are associated with the annihilation rate [12]. In this work, Eq. (9) will not be applied as the parameter  $\beta_1$  is assumed to be a constant value.

Movement of dislocations within the crystal lattice is blocked by two different types of barriers: short-range barrier and long-range barrier. The thermal activation energy can be used to overcome the former but cannot be used to overcome the latter. Because of this, several works [4, 17, 18] were able to demonstrate that the total flow stress ( $\sigma$ ) can be additively decomposed into the thermal ( $\sigma_{th}$ ) and athermal ( $\sigma_a$ ) components as follows:

$$\sigma = \sigma_a + \sigma_{th} \tag{11}$$

For the bcc crystalline structure in the current model, the athermal component  $\sigma_a(\epsilon_p)$  can be defined as a function of the equivalent plastic strain  $\epsilon_p$ , while the thermal component  $\sigma_{th}(\dot{\epsilon}_p, T)$  is dependent on equivalent plastic strain rate  $\dot{\epsilon}_p$  and temperature  $T$  as follows:

$$\sigma_a(\epsilon_p) = Y_a + B \epsilon_p^n \tag{12}$$

$$\sigma_{th}(\dot{\epsilon}_p, T) = Y_d \left(1 - \left(\beta_1 T - \beta_2 T \ln \frac{\dot{\epsilon}_p}{\dot{\epsilon}_p^0}\right)^{\frac{1}{q}}\right)^{\frac{1}{p}} \tag{13}$$

where  $Y_a$  represents the athermal yield stress, and the terms  $B$  and  $n$  describe the athermal hardening process. The thermal yield stress is represented by the term  $Y_d$ . In Sect. 3, the parameters for niobium employed in Eqs. (12) and (13) will be determined.

Further, increases in local temperature can be caused by inelastic dissipation through adiabatic heating under high deformation rates. Under dynamic loading, the temperature variation during the deformation process affects the crystal lattice structure of metals, known as thermal softening; this

effect is considered in Eq. (14). Under quasi-static loading, conduction and convection terms can dissipate any inelastic heating that may occur. Therefore, the deformation process may be assumed as an isothermal process. During dynamic deformation, adiabatic heating can cause an increase in the temperature; this increase in temperature can be calculated as follows [7]:

$$\Delta T = \frac{\beta}{c_p \bar{\rho}} \int_0^{\epsilon_p} \sigma d\epsilon_p \quad (14)$$

where  $\beta$  represents the Taylor–Quinney empirical coefficient and will be taken as 0.9 in this work as commonly assumed for most metals [19]. The term  $c_p$  represents the specific heat at constant pressure, and  $\bar{\rho}$  denotes the material density. To account for the adiabatic heating during plastic deformation, the temperature can be updated using Eq. (14). It is only necessary to consider the effects of thermal softening on the flow stress for dynamic loading conditions ( $\dot{\epsilon} = 3300 \text{ s}^{-1}$ ). Conversely, for quasi-static loading ( $\dot{\epsilon} = 0.001 \text{ s}^{-1}$ ), isothermal conditions can be assumed.

## 2.2 DSA Stress Components

Below the dislocation, atoms are more spread out, leading bulky solute atoms to congregate underneath the dislocations forming Cottrell atmospheres. These atmospheres restrict dislocations motion and hold them in place. This induces an increase in strength as dislocations arrested by their solute atmospheres are unable to move, and thus unable to produce plastic strain. This is the major process of DSA (Fig. 2). Thus, the mechanism that creates the DSA effect is related to the interaction between diffusing solute atoms and mobile dislocations [20]. During deformation, solute atoms are forced through the lattice structure creating mobile dislocations that

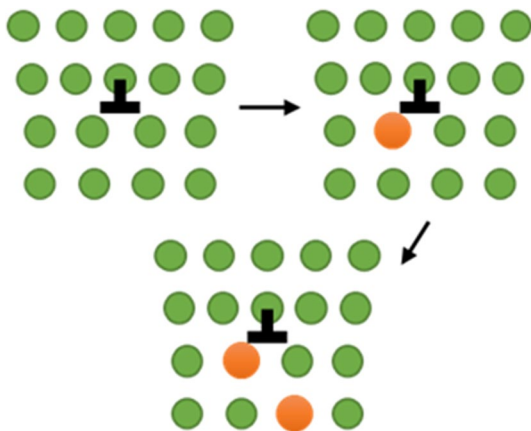


**Fig. 2** Schematic atomic positions during dynamic strain aging. The circles in orange color represent larger substitutional impurities, which are driven across the slip plane during dynamic strain aging. (Color figure online)

eventually become pinned at other dislocations. These mobile dislocations remain pinned until a sufficient level of flow stress is achieved to dislodge the dislocation. The amount of time that a dislocation remains pinned is known as the waiting time ( $t_w$ ). When  $t_w$  meets the aging time ( $t_a$ ), the strain hardening due to DSA occurs [21].

The dislocation density can be related to the equivalent plastic strain as follows [6]:

$$\frac{d\rho}{d\epsilon_p} = U - A - \Omega\rho \quad (15)$$

The dislocation density,  $\rho$ , in Eq. (15) can be calculated by

$$\rho = \frac{U - A}{\Omega} [1 - \exp(-\Omega\epsilon_p)] + \rho_0 \exp(-\Omega\epsilon_p) \quad (16)$$

where  $\rho_0$  represents the initial dislocation density.

Bergstrom and Roberts [6] investigated the effects of DSA on flow stress through the comparison of experiments and model predictions as shown in Fig. 3. The data shows an increase in yield stress at certain temperature ranges caused by a combination of a large  $U - A$  value and a low  $\Omega$  value. The resulting increase in the flow stress can be expressed by substituting Eq. (16) into Taylor's dislocation model [22] ( $\sigma = \alpha\mu b\sqrt{\rho}$ , where  $\alpha$  is the material constant and  $\mu$  is the shear modulus).

$$\sigma = \sigma_0 + \alpha\mu b \left\{ \frac{U - A}{\Omega} [1 - \exp(-\Omega\epsilon_p)] + \rho_0 \exp(-\Omega\epsilon_p) \right\}^{1/2} \quad (17)$$

where  $\sigma_0$  is the strain independent friction stress. This leads to the conclusion that DSA is a phenomenon with a probabilistic nature and it may be modeled using probability function.

To model the probabilistic nature of the DSA phenomenon, the term  $\sigma_D$  is introduced to model the bell-shaped hardening. By assuming  $\sigma_D(\epsilon_p, \dot{\epsilon}_p, T)$ , the proposed model can be expressed as follows:

$$\sigma_{PMI,II}(\epsilon_p, \dot{\epsilon}_p, T) = \sigma_a(\epsilon_p) + \sigma_{th}(\dot{\epsilon}_p, T) + \sigma_D(\epsilon_p, \dot{\epsilon}_p, T) \quad (18)$$

where Eqs. (12) and (13) define the two components  $\sigma_a$  and  $\sigma_{th}$  respectively.

In this work, the DSA component is modeled by two mathematical models. The first one, Proposed Model (PM I), was employed in the authors' previous works [9–12]. The second one, Proposed Model (PM II), was put forth by the work of Wang et al. [23]. Both models are employed in this work to describe the hardening induced by DSA.

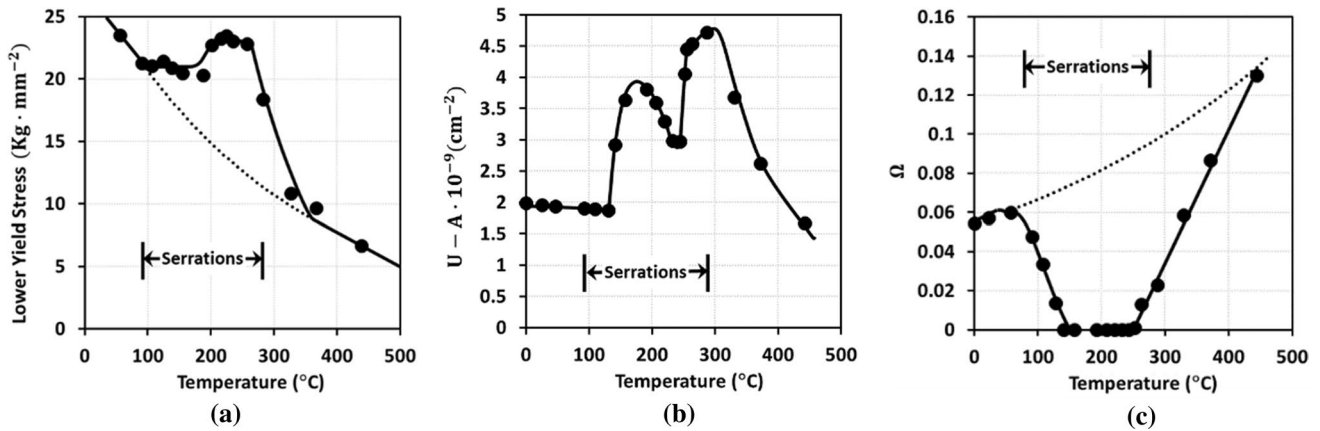


**Fig. 3** Experimental data (dots) are graphed against model predictions (lines) as a function of temperature: **a** lower yield stress, **b**  $U - A$  and **c**  $\Omega$  [6]

**2.2.1 Proposed Model I**

In the works [9–12], the Weibull distribution probability density function characterizes  $\sigma_D$  with the following expression:

$$\sigma_D(\epsilon_p, \dot{\epsilon}_p, T) = a_D(\epsilon_p) \exp \left[ - \frac{\{T - \mathcal{W}(\dot{\epsilon}_p)\}^2}{b_D(\epsilon_p)} \right] \quad (19)$$

where the terms  $a_D > 0$  and  $b_D > 0$  define the shape and scale of  $\sigma_D$ . The term  $\mathcal{W}$  is defined by the temperature where the relationship between solute atoms and mobile dislocations becomes the strongest. In this work, power-law functions are applied for  $a_D$ ,  $b_D$ , and  $\mathcal{W}$ , i.e.  $a_D(\epsilon_p) = k_a \epsilon_p^{n_a}$ ,  $b_D(\epsilon_p) = k_b \epsilon_p^{n_b}$ , and  $\mathcal{W}(\dot{\epsilon}_p) = k_{\mathcal{W}} \dot{\epsilon}_p^{n_{\mathcal{W}}}$ . However, other types of functions can also be used [9, 12]. In Sect. 3, the material constants ( $k_a$ ,  $k_b$ , and  $k_{\mathcal{W}}$ ) and the law’s exponents ( $n_a$ ,  $n_b$ , and  $n_{\mathcal{W}}$ ) are established by comparing the model with the experimental data. The function  $b_D$  defines the temperature range at which DSA hardening occurs.

**2.2.2 Proposed Model II**

In Wang et al. [23], the effect of DSA with the identical functional form presented in Eq. (19) was modeled. However, the terms,  $a_D$ ,  $b_D$  and  $\mathcal{W}$ , were all defined as functions of not only the equivalent plastic strain  $\epsilon_p$  but also the plastic strain rate  $\dot{\epsilon}_p$ , i.e.  $a_D(\epsilon_p, \dot{\epsilon}_p)$ ,  $b_D(\epsilon_p, \dot{\epsilon}_p)$  and  $\mathcal{W}(\epsilon_p, \dot{\epsilon}_p)$ , as follows:

$$a_D(\epsilon_p, \dot{\epsilon}_p) = \left( \bar{a}_D \ln \frac{\dot{\epsilon}_p}{\dot{\zeta}} + \bar{a}_D \right) \epsilon_p^{n_2} \quad (20)$$

$$b_D(\epsilon_p, \dot{\epsilon}_p) = \left( \frac{T_2}{\ln \frac{\dot{\epsilon}_p}{\dot{\zeta}} - \eta \ln \frac{\epsilon_p}{\epsilon_p^0}} \right)^2 \quad (21)$$

$$\mathcal{W}(\epsilon_p, \dot{\epsilon}_p) = \frac{T_1}{\ln \frac{\dot{\epsilon}_p}{\dot{\zeta}} - \eta \ln \frac{\epsilon_p}{\epsilon_p^0}} \quad (22)$$

where the material constants  $\bar{a}_D$ ,  $\bar{a}_D$ ,  $\dot{\zeta}$ ,  $n_3$ ,  $T_1$ ,  $T_2$ ,  $\eta$ , and  $\epsilon_p^0$  should be calibrated using experimental data. Detailed derivations of these constants Eqs. (20)–(22) are discussed in detail by Wang et al. [23].

**3 Calibration and Validation for the Proposed Models**

**3.1 Athermal and Thermal Stress Components**

To accurately calibrate the constants for these models, the stress-temperature curves for various strain rates and total strain levels from the experimental data are examined. As discussed previously, flow stress tends to decrease with a rise in temperature until a critical temperature value is reached. After this critical temperature is reached, flow stress remains constant with temperature. The constant flow stress at this critical temperature is indicative of the athermal component of the flow stress,  $\sigma_a$ . By examining the experimental data provided by Nemat-Nasser and Guo [1], the material parameters ( $Y_a$ ,  $B$ , and  $n$ ) in Eq. (12) can be approximated. The parameter  $Y_a$  represents the athermal flow stress in the elastic deformation zone, specifically at the initial yield ( $\epsilon_p = 0$ ). Because this study aims to model the plastic behavior of niobium, this parameter is set as zero. Figure 4 shows the athermal stress–strain curves for both the model predictions and experimental data (after refinement of material parameters) for comparison.

To compute the flow stress due to the thermal component  $\sigma_{th}$ , the total flow stress needs to be divided by substituting the athermal component and the DSA

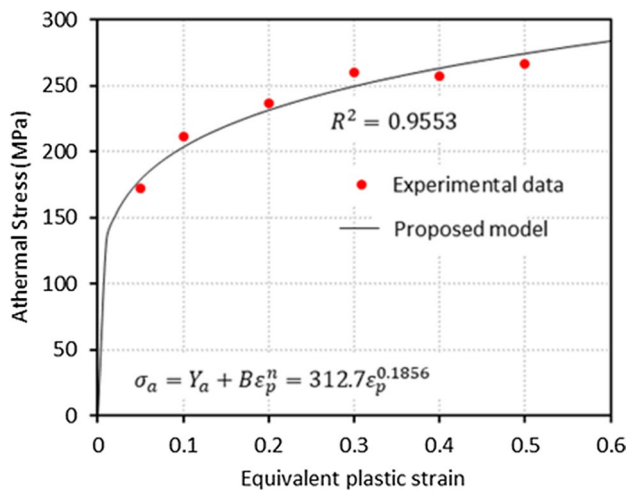


**Fig. 4** Comparison of flow stress due to the athermal component versus strain from the experiments [1] and the proposed model

component, i.e.  $\sigma_{th} = \sigma - \sigma_a - \sigma_D$ . By determining the appropriate values of  $p$  and  $q$ , the thermal degradation mechanism can be adequately modeled. These parameters generally fall within the following ranges:  $0 \leq p \leq 1$  and  $1 \leq q \leq 2$ . The values of  $p = 0.15$  and  $q = 1.95$  were found to produce the most accurate predictions in the present work. The thermal yield stress  $Y_d$  is defined by the flow stress at initial yield point  $\sigma_{\epsilon_p=0}$ . To calculate  $Y_d$ , Eqs. (12) and (13) are employed to plot  $(\sigma_{\epsilon_p=0} - Y_a)^p$  versus  $T^{-\frac{1}{q}}$  for each strain rate. To determine  $\beta_1$  and  $\beta_2$ ,

the  $(1 - ((\sigma_{\epsilon_p=0} - Y_a)/Y_d)^p)^q$  versus  $\dot{\epsilon}_p$  graphs at certain temperatures are used.

Utilizing the equations discussed above, the thermal flow stress component,  $\sigma_{th}$ , can be calibrated by comparing the model predictions with the experimental data as shown in Fig. 5. It is important to mention that the graphed curve remains identical regardless of the magnitude of the plastic strain, and this demonstrates that the thermal stress component  $\sigma_{th}$  in the bcc crystalline structure is independent of plastic strain, unlike fcc. The dots used in Fig. 5 are from the experimental data and are obtained by subtracting the athermal stresses (Fig. 4) from the total stresses. The material parameters in Table 1 were obtained for the athermal and thermal components of the VA model for niobium.

### 3.2 DSA Stress Components

To properly capture the behavior of DSA-induced flow stress with the constitutive model, the expressions for  $a_D$ ,  $b_D$  and  $\mathcal{W}$  must be well defined. The experiments conducted by Nemat-Nasser and Guo [1] at the strain rates of  $\dot{\epsilon} = 0.001 \text{ s}^{-1}$  and  $3300 \text{ s}^{-1}$  show the bell-shaped curve on the flow stresses produced by DSA and the data from these experiments are used to define these expressions.

#### 3.2.1 Proposed Model I (PM I)

The parameters  $a_D$  and  $b_D$  can be defined by comparing the experimental data with the increase in flow stress due

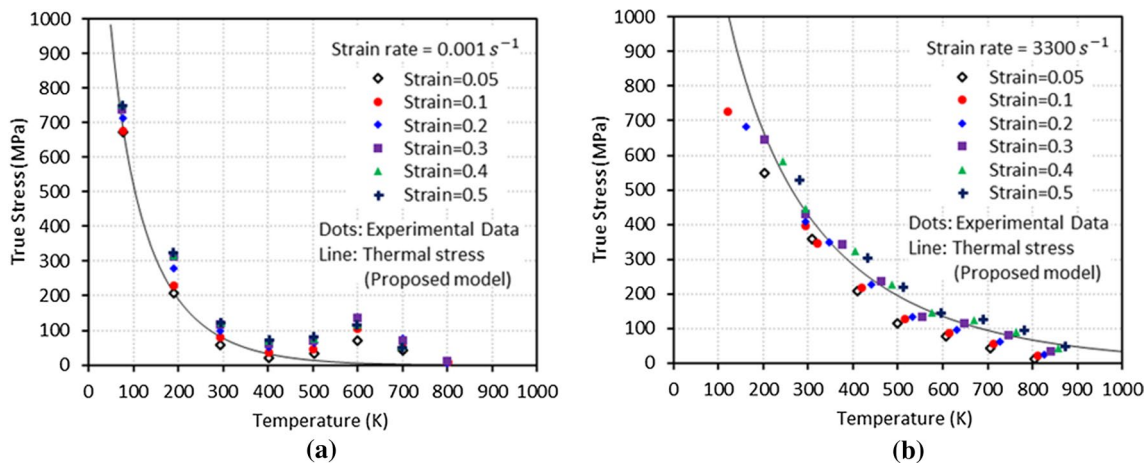


**Fig. 5** Comparison of true flow stress versus temperature curves predicted by the VA model (Eq. 13) with data from the experiments [1]: **a**  $\dot{\epsilon} = 0.001 \text{ s}^{-1}$  and **b**  $\dot{\epsilon} = 3300 \text{ s}^{-1}$

**Table 1** Model parameters for niobium employed by the VA model

$Y_a$ (MPa)	$B$ (MPa)	$n$ (-)	$Y_d$ (MPa)	$\beta_1$ (1/K)	$\beta_2$ (1/K)	$p$ (-)	$q$ (-)	$\dot{\epsilon}_p^0$ ( $\text{s}^{-1}$ )
0	312.7	0.1856	3500	$7.8 \times 10^{-4}$	$2.65 \times 10^{-5}$	0.15	1.95	$1.0 \times 10^{-5}$

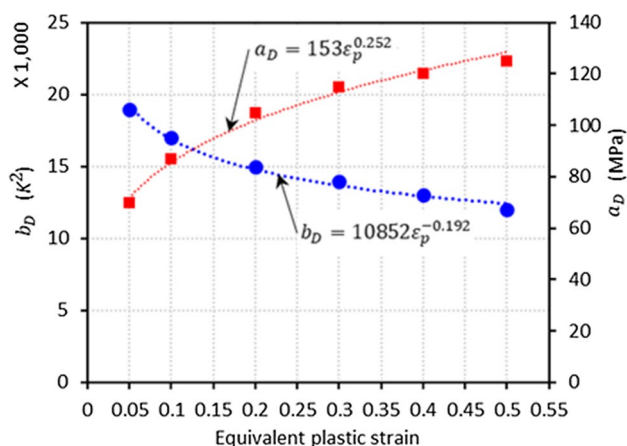


**Fig. 6** Plots of  $a_D$  and  $b_D$  versus  $\epsilon_p$  with trend lines derived by using a power-law form. The dots represent values obtained from the experimental results [1]

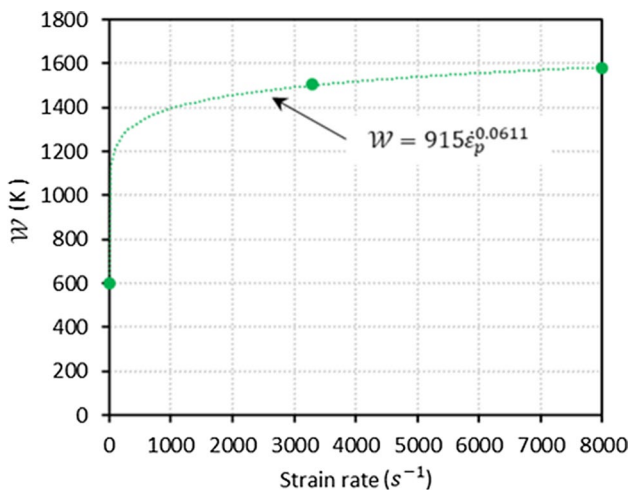


**Fig. 7** Plot of  $W$  as a function of  $\dot{\epsilon}_p$ . The dots represent values obtained from the experimental results [1]

to DSA predicted by Eq. (19) as revealed in Fig. 6. Further information is provided in the authors’ previous works [9–12] on defining the parameters’ functional forms. The expressions for  $a_D$  and  $b_D$  are expressed as functions of the equivalent plastic strain as follows:

$$a_D(\epsilon_p) = 153\epsilon_p^{0.252} (MPa) \tag{23}$$

$$b_D(\epsilon_p) = 10852\epsilon_p^{-0.192} (K^2) \tag{24}$$

Conversely,  $W$  is a function of the strain rate. The expression for  $W$  can be derived in a similar fashion as used for the parameters  $a_D$  and  $b_D$  as follows (see Fig. 7):

$$W(\dot{\epsilon}_p) = 915\dot{\epsilon}_p^{0.0611} (K) \tag{25}$$

By combining Eqs. (23), (24) and (25) into Eq. (19), the PM1 mathematical expression for the DSA-induced flow stress is derived as follows:

$$\sigma_{DPM1}(\epsilon_p, \dot{\epsilon}_p, T) = 153\epsilon_p^{0.252} \exp\left[-\frac{\left\{T - 915\dot{\epsilon}_p^{0.0611}\right\}^2}{10852\epsilon_p^{-0.192}}\right] \tag{26}$$

In Fig. 8, the hardening caused by DSA can be seen according to the variation of temperature at various designated strain levels. PM I shows consistency with the experimental data captured under both quasi-static loading and dynamic loading.

The VA model and PM I predictions of the true stress-temperature responses are displayed in Figs. 9 and 10. The model predictions are compared to the experimental data at designated total strains and strain rates. It can be seen in the figures that the VA model is not able to account for the DSA induced hardening, on the other hand, the PM I shows

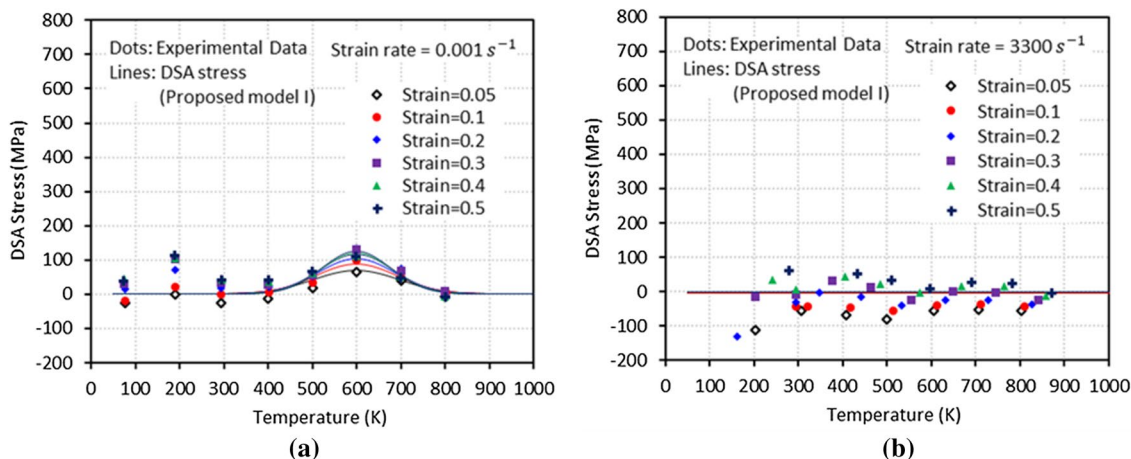


**Fig. 8** Comparison between PM I predictions of additional flow stress caused by DSA and the experimental results [1]: **a**  $\dot{\epsilon} = 0.001 \text{ s}^{-1}$  and **b**  $\dot{\epsilon} = 3300 \text{ s}^{-1}$

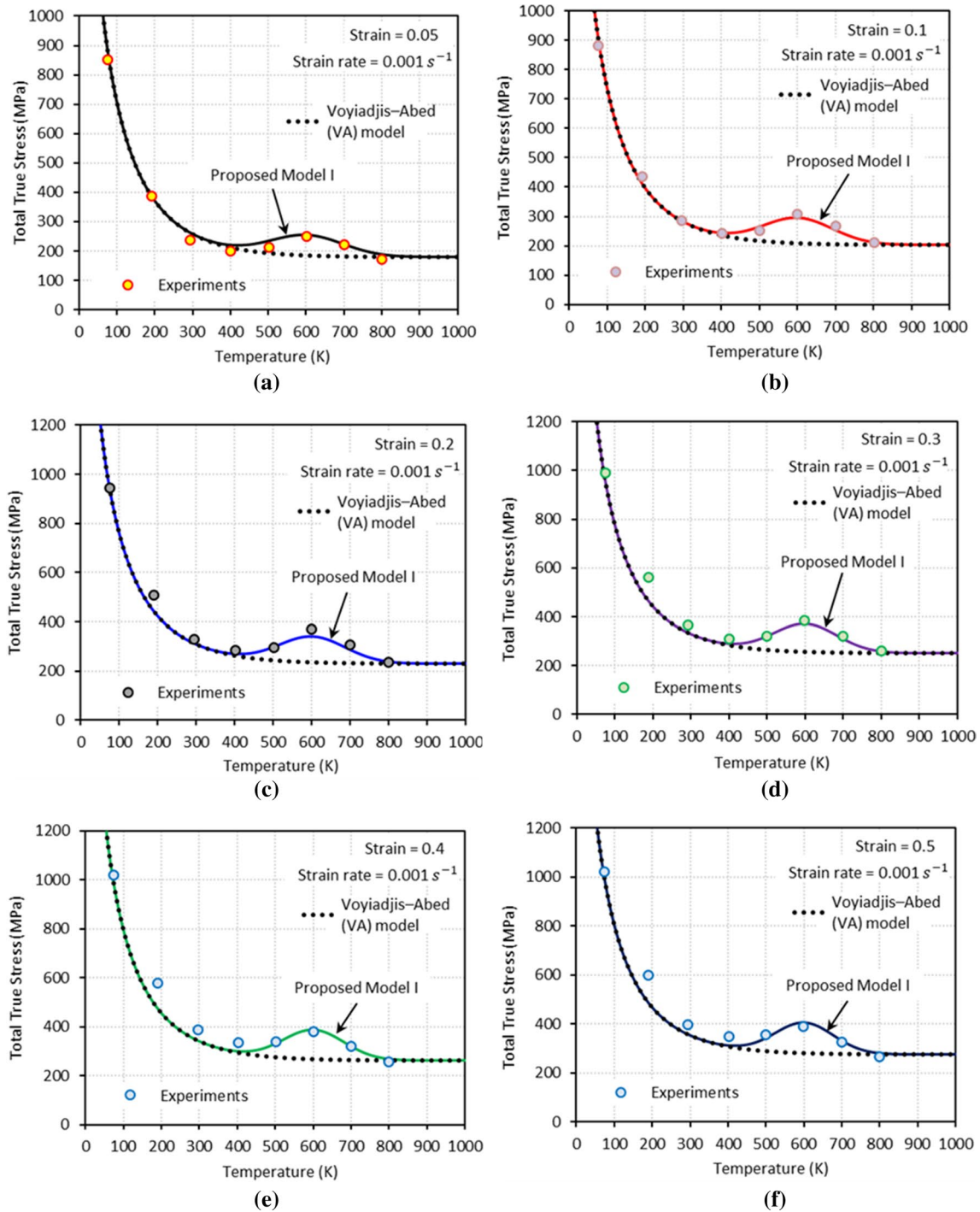


**Fig. 9** The VA model and proposed Model I predictions of total true stress versus temperature displayed along with the experimental results [1] at **a**  $\epsilon = 0.05$ , **b**  $\epsilon = 0.1$ , **c**  $\epsilon = 0.2$ , **d**  $\epsilon = 0.3$ , **e**  $\epsilon = 0.4$  and **f**  $\epsilon = 0.5$ . The quasi-static strain rate,  $\dot{\epsilon} = 0.001 \text{ s}^{-1}$ , is applied

sufficient predictions of the effects of DSA under quasi-static loading. Additionally, the PM I is also capable of capturing the experimental results in dynamic loading cases where no DSA effect is observed.

### 3.2.2 Proposed Model II (PM II)

For the PM II, the DSA effect is approximated using Eqs. (20)–(22) along with Eq. (19). Table 2 summarizes the model parameters for niobium used in the PM II.

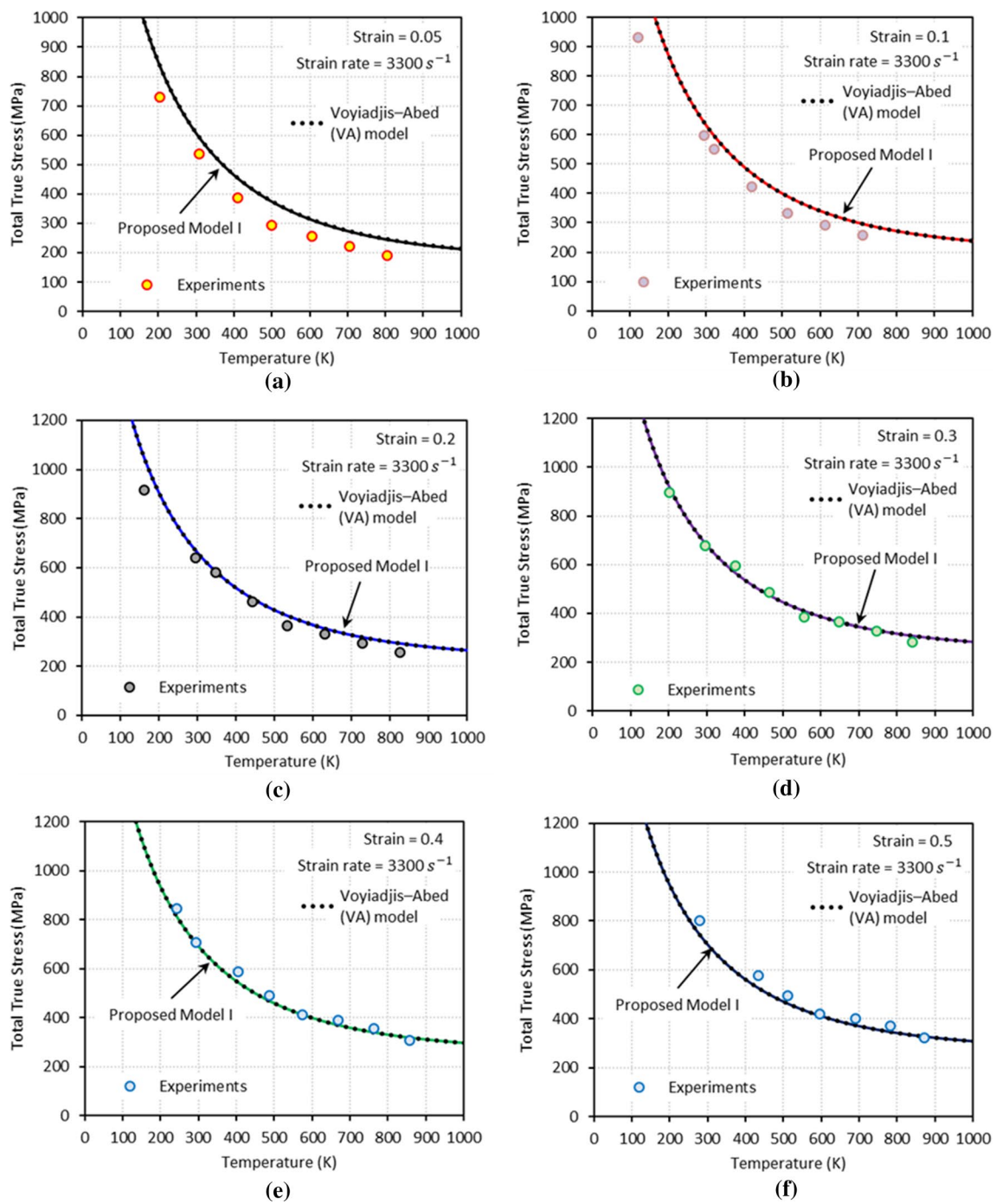


**Fig. 10** The VA model and proposed Model I predictions of total true stress versus temperature displayed along with the experimental results [1] at **a**  $\epsilon = 0.05$ , **b**  $\epsilon = 0.1$ , **c**  $\epsilon = 0.2$ , **d**  $\epsilon = 0.3$ , **e**  $\epsilon = 0.4$  and **f**  $\epsilon = 0.5$ . The dynamic strain rate,  $\dot{\epsilon} = 3300 \text{ s}^{-1}$ , is applied

**Table 2** Model parameters for niobium employed in the PM II

$\bar{a}_D$ (MPa)	$\bar{a}_D$ (MPa)	$n_2$ (-)	$\zeta$ (/s)	$T_1$ (K)	$T_2$ (K)	$\eta$ (-)	$\epsilon_p^0$ (-)
-5	10	0.22	$6.5 \times 10^{10}$	-19,500	-4000	-0.35	1.0

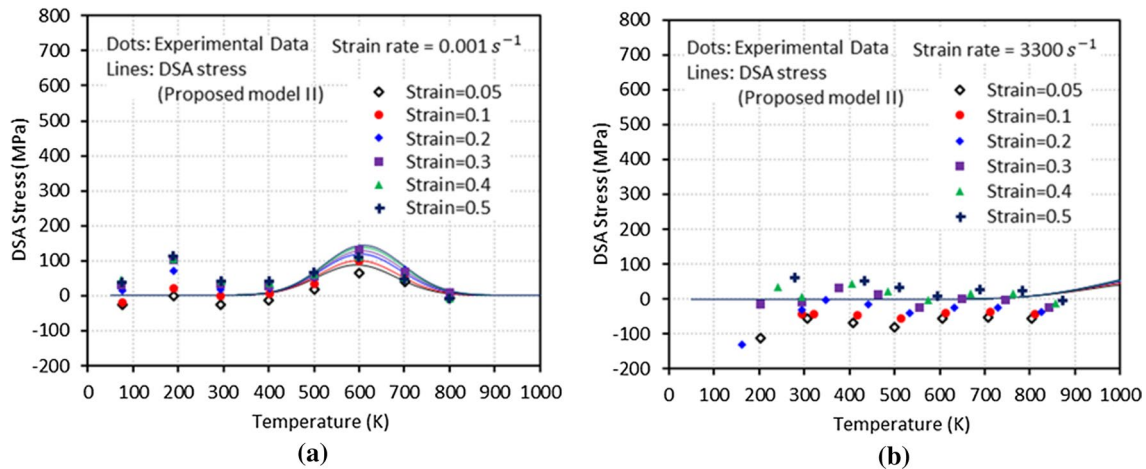


**Fig. 11** Comparison between PM II predictions of additional flow stress caused by DSA and the experimental results [1]: **a**  $\dot{\epsilon} = 0.001 \text{ s}^{-1}$  and **b**  $\dot{\epsilon} = 3300 \text{ s}^{-1}$

After using the abovementioned equations and the parameters from Table 2, PM II is defined as follows:

$$\sigma_{DPMII}(\epsilon_p, \dot{\epsilon}_p, T) = \left[ \left( \bar{a}_D \ln \frac{\dot{\epsilon}_p}{\dot{\epsilon}_0} + \bar{a}_D \right) \epsilon_p^{n_2} \right] \exp \left[ - \left\{ \frac{T - \frac{T_1}{\ln \frac{\dot{\epsilon}_p}{\dot{\epsilon}_0} - \eta \ln \frac{\dot{\epsilon}_p}{\dot{\epsilon}_0}}}{\frac{T_2}{\ln \frac{\dot{\epsilon}_p}{\dot{\epsilon}_0} - \eta \ln \frac{\dot{\epsilon}_p}{\dot{\epsilon}_0}}} \right\}^2 \right] \quad (27)$$

Similar to PM I, PM II models the bell-shaped DSA hardening effect and can capture the experimental data as shown in Fig. 11 under both quasi-static and dynamic loading. The difference between PM I and PM II is the ability of PM II to predict the DSA behavior beyond  $T = 800 \text{ K}$  under dynamic loading. The DSA phenomenon cannot be detected by PM I in this temperature range. Without further experimental data in this temperature range, it is not possible to discern which model is correct.

The VA model and PM II predictions of total true stress-temperature curves are shown in Figs. 12 and 13 concurrently with the experimental data under varying strain levels and applied strain rates. The flow stress predictions made by the PM II follow the experimental data closely including the DSA phenomenon under quasi-static loading. Figure 13 shows the PM II predictions for DSA-induced hardening beyond  $T = 800 \text{ K}$ . To verify the validity of the PM II predictions in this temperature range, further experimental data will be required.

#### 4 Stress–Strain Curves

To verify the accuracy of the proposed models, this section will be dedicated to true stress-true strain behaviors. The DSA induced hardening is not captured in the stress–strain

curves produced in the model proposed by Voyiadjis and Abed [7].

The true stress versus true strain curves produced by both PM I and PM II are compared to the experiments [1] in Figs. 14 and 15 for the strain rates of  $\dot{\epsilon} = 0.001 \text{ s}^{-1}$  and  $\dot{\epsilon} = 3300 \text{ s}^{-1}$ . When DSA becomes active, the VA model does not accurately predict the behavior of the stress–strain responses, i.e.  $\dot{\epsilon} = 0.001 \text{ s}^{-1}$  with  $T = 600 \text{ K}$  in Fig. 14a. On the other hand, both the PM I and PM II produce predictions that follow the experimental data closely.

Figures 16 and 17 show the flow stress surfaces produced by PM I and PM II under quasi-static and dynamic strain rates ( $\dot{\epsilon} = 0.001 \text{ s}^{-1}$  and  $3300 \text{ s}^{-1}$ ) with a temperature range between 0 to 1000 K and a strain range from 0.05 to 0.4. The experimental data is illustrated by dots on the figures. The proposed models produce surfaces that fall near or mostly near the experimental results in all cases.

#### 5 Strain Rate Sensitivity

DSA is related to spatio-temporal instabilities. To study these instabilities, the strain rate sensitivity (SRS), expressed by  $m = \partial \log \sigma / \partial \log \dot{\epsilon}$ , is regarded as a major factor as reported in Fressengeas and Molinari [24]. Materials with a negative SRS caused by DSA may cause instabilities quicker than materials with a positive SRS. This phenomenon is caused by the relationship between strain hardening, temperature sensitivity, and strain rate sensitivity as illustrated by Fressengeas and Molinari [24].

In Fig. 18, the total true stress versus strain rate responses from the VA model, PM I and PM II are plotted. In this figure, the experimental data are represented by dots. The VA model illustrates a positive SRS ( $m > 0$ ), and the PM I

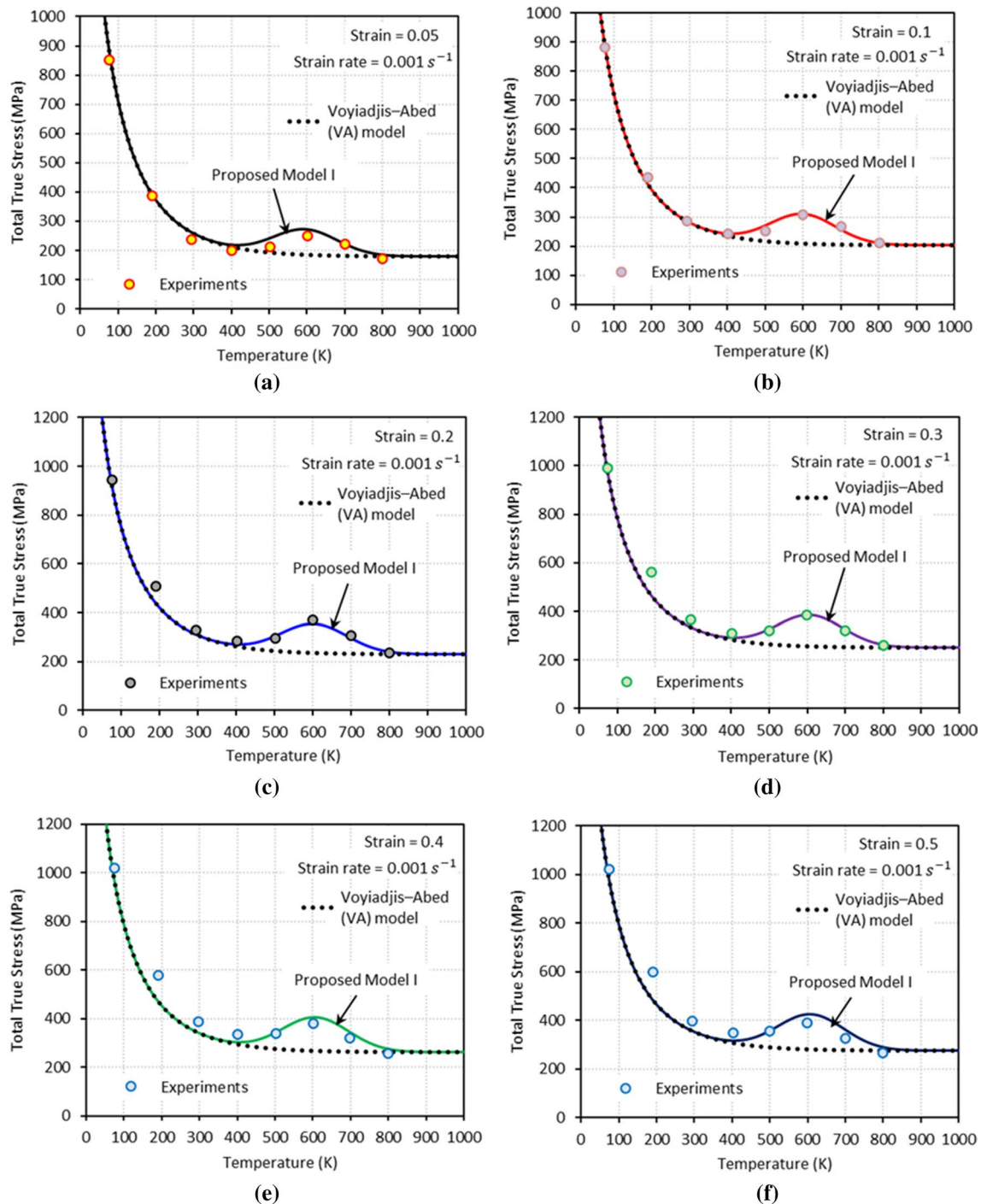


**Fig. 12** The VA model and proposed Model II predictions of total true stress versus temperature displayed along with the experimental results [1] at **a**  $\epsilon = 0.05$ , **b**  $\epsilon = 0.1$ , **d**  $\epsilon = 0.2$ , **d**  $\epsilon = 0.3$ , **e**  $\epsilon = 0.4$  and **f**  $\epsilon = 0.5$ . The quasi-static strain rate,  $\dot{\epsilon} = 0.001 \text{ s}^{-1}$ , is applied

and PM II illustrate a negative SRS in the certain ranges of  $(T, \dot{\epsilon})$ . The PM I and PM II give agreeable predictions with the experimental data, when DSA is active ( $T = 600 \text{ K}$ ), whereas the VA model does not give an accurate prediction.

## 6 Conclusions

Constitutive modeling for the plastic deformation of niobium was carried out at a broad range of strain rates and temperatures. The proposed model includes the effect of dynamic strain aging-induced hardening by means of the

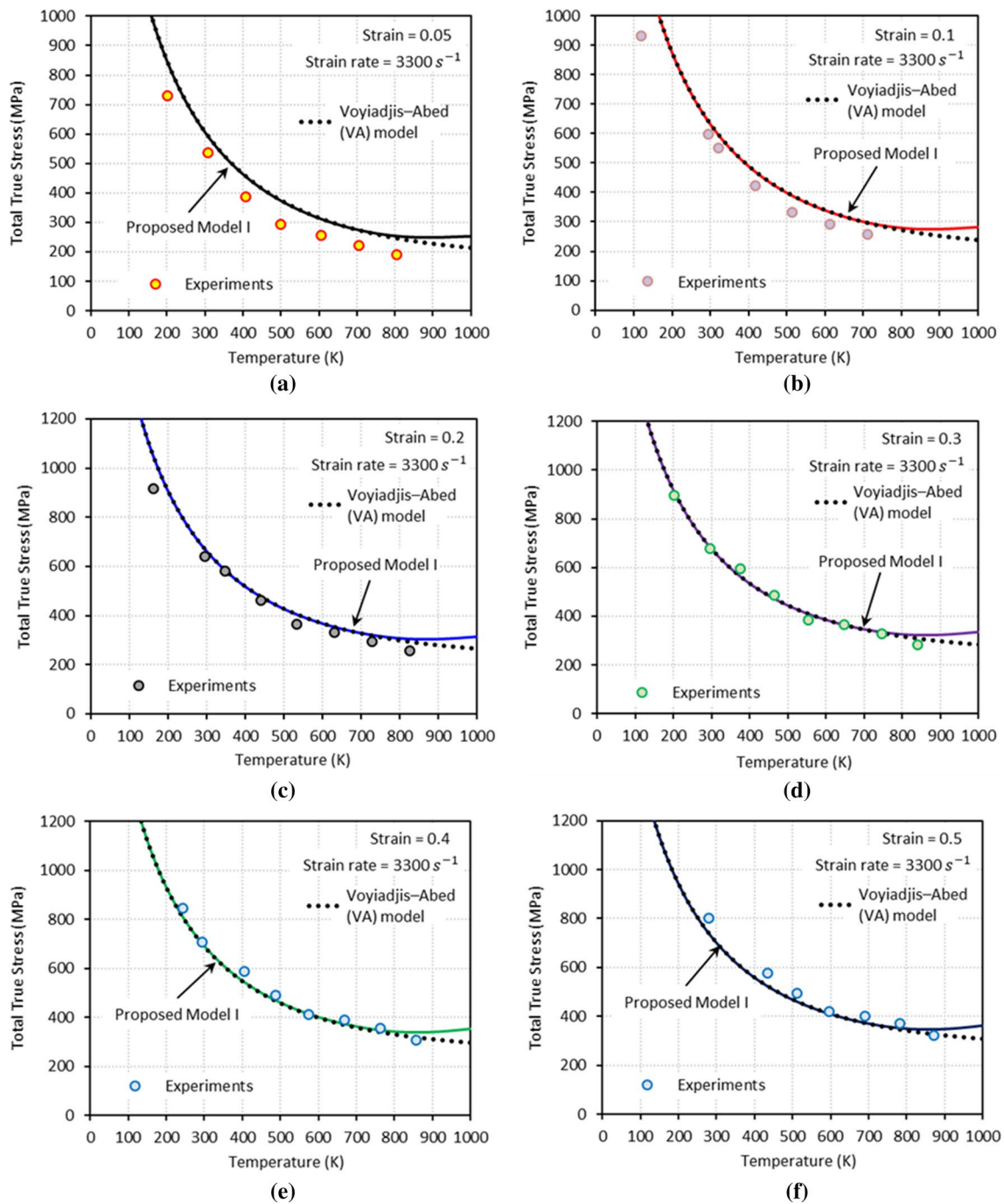


**Fig. 13** The VA model and proposed Model II predictions of total true stress versus temperature displayed along with the experimental results [1] at **a**  $\varepsilon = 0.05$ , **b**  $\varepsilon = 0.1$ , **c**  $\varepsilon = 0.2$ , **d**  $\varepsilon = 0.3$ , **e**  $\varepsilon = 0.4$  and **f**  $\varepsilon = 0.5$ . The dynamic strain rate,  $\dot{\varepsilon} = 3300 \text{ s}^{-1}$ , is applied

new mathematical formulations. Some noticeable outcomes of the current work are summarized below.

- In the experiments regarding niobium, the bell-shaped hardening due to DSA in stress–temperature curves was observed at a low strain rate ( $\dot{\varepsilon} = 0.001 \text{ s}^{-1}$ ), but not observed at a high strain rate ( $\dot{\varepsilon} = 3300 \text{ s}^{-1}$ ).
- To capture the DSA-induced hardening, two constitutive models (PM I and PM II) were proposed in this work, and compared with the old model (VA model). It was found that the DSA-induced hardening cannot be captured by the VA model.

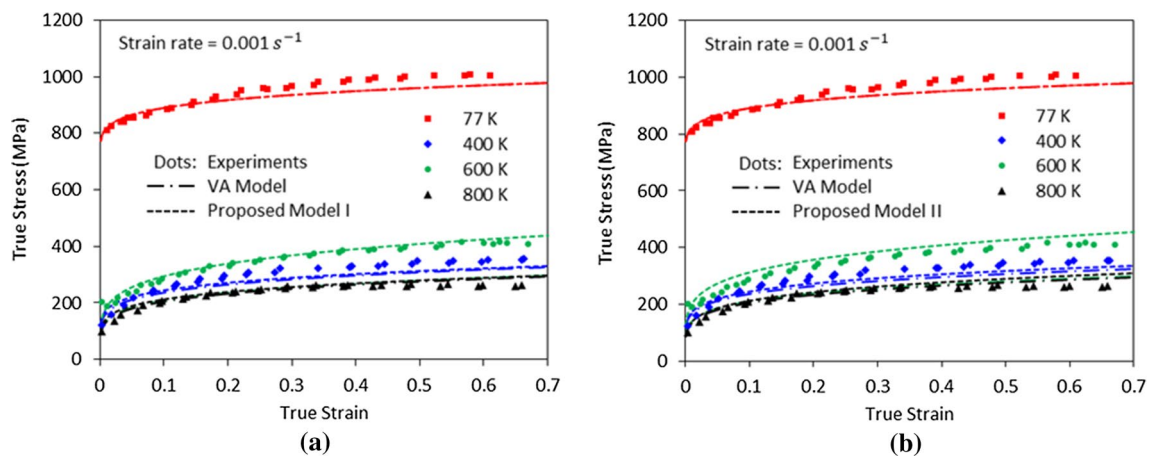


**Fig. 14** Predictions of true stress–true strain curves under quasi-static loading ( $\dot{\epsilon} = 0.001 \text{ s}^{-1}$ ) by the VA model, **a** PM I and **b** PM II and experimental data Nemat-Nasser and Guo [1]

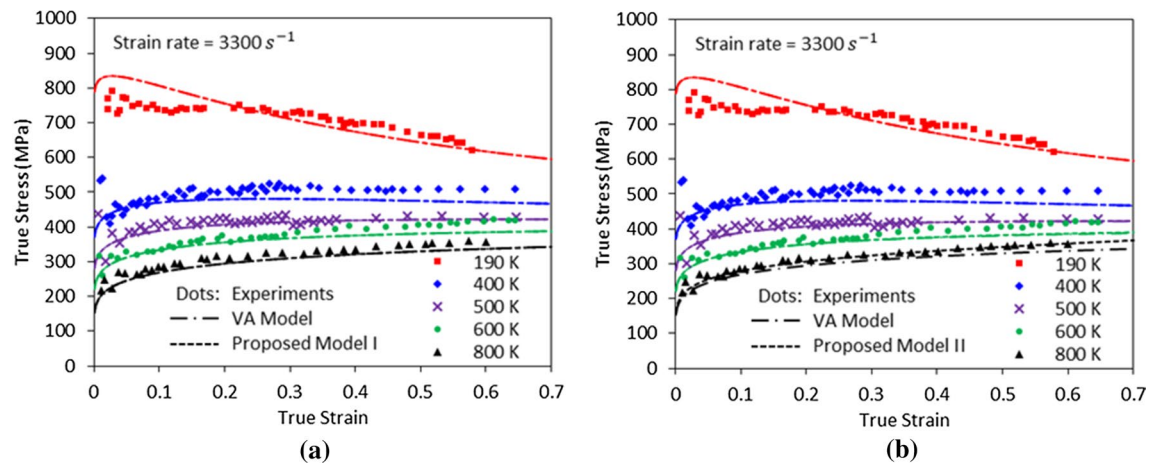


**Fig. 15** Predictions of true stress–true strain curves under dynamic loading ( $\dot{\epsilon} = 3300 \text{ s}^{-1}$ ) by the VA model, **a** PM I, **b** PM II and experimental data Nemat-Nasser and Guo [1]

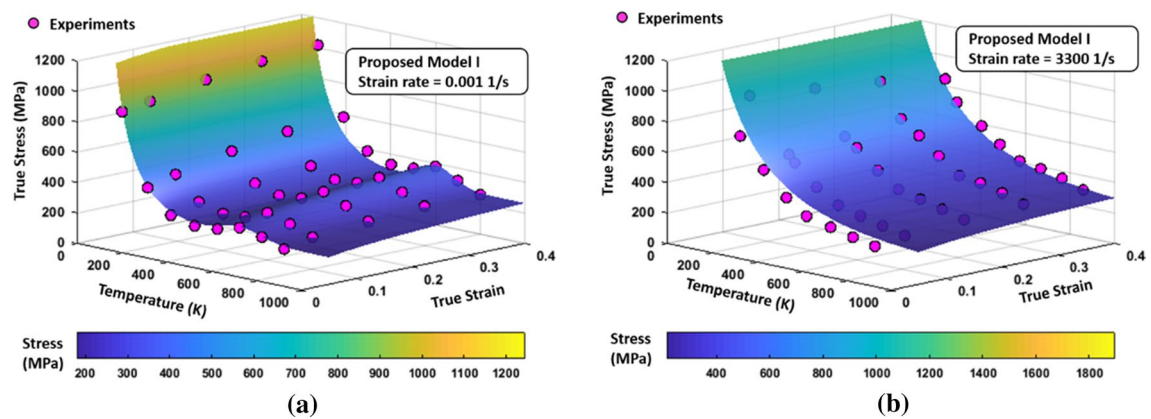


**Fig. 16** Flow stress surfaces predicted by the PM I at a wide range of temperature and strain with **a**  $\dot{\epsilon} = 0.001 \text{ s}^{-1}$  and **b**  $\dot{\epsilon} = 3300 \text{ s}^{-1}$ . The experimental data are from Nemat-Nasser and Guo [1]

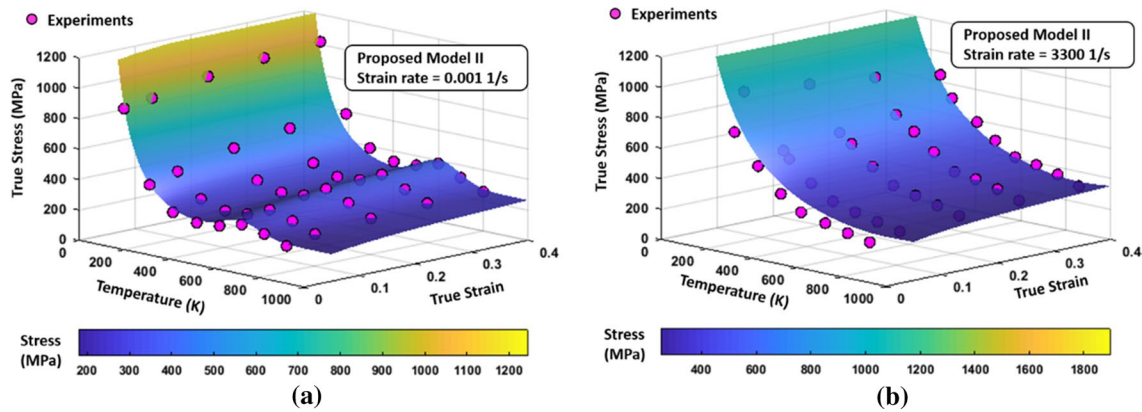


**Fig. 17** Flow stress surfaces predicted by the PM II at a wide range of temperature and strain with **a**  $\dot{\epsilon} = 0.001 \text{ s}^{-1}$  and **b**  $\dot{\epsilon} = 3300 \text{ s}^{-1}$ . The experimental data are from Nemat-Nasser and Guo [1]

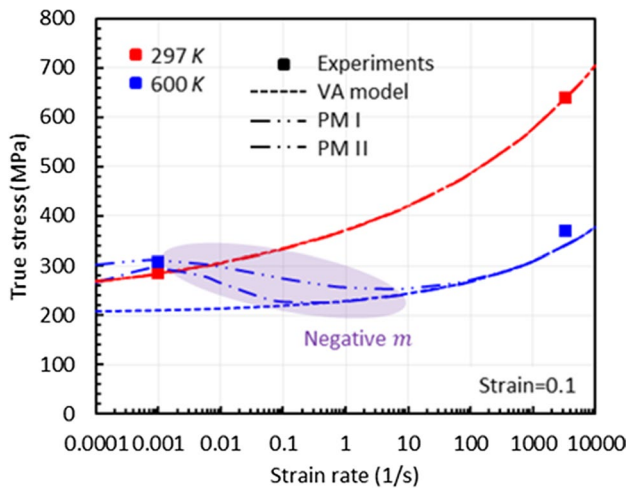


**Fig. 18** Graph of true stress as a function of strain rate for temperatures, 297 K and 600 K, at  $\epsilon=0.1$ . Dots indicate the experimental data from Nemat-Nasser and Guo [1]

- Both the PM I and PM II, on the other hand, provide agreeable predictions with the inclusion of the DSA effect at all strain rate ranges.
- In addition, both the PM I and PM II were able to capture the negative strain rate sensitivity due to DSA, which is not the case in the VA model.
- Based on the findings of the current work, finite element algorithms for the proposed models will be developed and applied to shear band simulations and necking problems to investigate instabilities in the future.

## References

1. S. Nemat-Nasser, W.G. Guo, *Mater. Sci. Eng. A-Struct.* **284**, 202–210 (2000)
2. S. Nemat-Nasser, Y. Li, *Acta Mater.* **46**, 565–577 (1998)
3. S. Nemat-Nasser, W.G. Guo, *Mech. Mater.* **32**, 243–260 (2000)
4. S. Nemat-Nasser, J.B. Isaacs, *Acta Mater.* **45**, 907–919 (1997)
5. A. Keh, Y. Nakada, W. Leslie, *Dislocation Dynamics* (McGraw Hill, London, 1968), pp. 81–87
6. Y. Bergstrom, W. Roberts, *Acta Metall. Mater.* **19**, 1243–1251 (1971)
7. G.Z. Voyiadjis, F.H. Abed, *Mech. Mater.* **37**, 355–378 (2005)
8. A. Rusinek, J.R. Klepaczko, *Int. J. Plasticity* **17**, 87–115 (2001)
9. G.Z. Voyiadjis, Y. Song, A. Rusinek, *Mech. Mater.* **129**, 352–360 (2019)
10. Y. Song, D. Garcia-Gonzalez, A. Rusinek, *Materials* **13**, 1794 (2020)
11. Y. Song, G.Z. Voyiadjis, *Eur. J. Mech. A-Solid* **83**, 104034 (2020)
12. G.Z. Voyiadjis, Y. Song, *Acta Mech.* **231**, 19–34 (2020)
13. D.J. Bammann, E.C. Aifantis, *Acta Mech.* **45**, 91–121 (1982)
14. J. R. Klepaczko, in *Constitutive Relations and Their Physical Basis*, ed. by S.I. Andersen, J.B. Bilde-Sorensen, N. Hansen, T. Leffers, H. Lilholt, O.B. Pedersen, B. Ralph. the 8th Risø International Symposium on Metallurgy and Materials Science, Roskilde, September 7-11, 1987. (Risø National Laboratory, Roskilde, 1987), pp. 387–395
15. S. Arrhenius, *Z. Phys. Chem.* **4**, 96–116 (1889)
16. U.F. Kocks, A.S. Argon, M.F. Ashby, *Prog. Mater. Sci.* **19**, 1–281 (1975)
17. S. Nemat-Nasser, W.G. Guo, J.Y. Cheng, *Acta Mater.* **47**, 3705–3720 (1999)
18. F.J. Zerilli, R.W. Armstrong, *J. Appl. Phys.* **61**, 1816–1825 (1987)
19. D. Rittel, L.H. Zhang, S. Osovski, *J. Mech. Phys. Solids* **107**, 96–114 (2017)
20. A.H. Cottrell, *Philos. Mag.* **44**, 829–832 (1953)
21. P.G. McCormick, *Acta Metall. Mater.* **36**, 3061–3067 (1988)
22. G.I. Taylor, *J. Inf. Met.* **62**, 307–324 (1938)
23. J.J. Wang, W.G. Guo, X.S. Gao, J. Su, *Int. J. Plasticity* **65**, 85–107 (2015)
24. C. Fressengeas, A. Molinari, *J. Mech. Phys. Solids* **35**, 185–211 (1987)

**Publisher's Note** Springer Nature remains neutral with regard to jurisdictional claims in published maps and institutional affiliations.